

Charge-Transfer Effects of Organic Ligands on Energy Storage Performance of Oxide Nanoparticle-Based Electrodes

Yongkwon Song, Seokmin Lee, Yongmin Ko, June Huh, Yongju Kim, Bongjun Yeom, Jun Hyuk Moon, and Jinhan Cho*

One of the most difficult challenges related to pseudocapacitive nanoparticle (PC NP)-based energy storage electrodes with theoretically high capacity is to overcome the sluggish charge-transfer kinetics that result from the poorly conductive PC NPs and bulky/insulating organics (i.e., organic ligands and/or polymeric binders) within the electrodes. Herein, it is reported that physical/chemical functionalities of organic ligands and their molecular-scale coating onto NPs have considerable effects on the rate capability and capacity of oxide NP-based pseudocapacitor electrodes. For this study, pseudocapacitive iron oxide (Fe_3O_4) NPs are layer-by-layer (LbL)-assembled with conductive indium tin oxide (ITO) NPs using various types of organic ligands (or linkers). In particular, hydrazine ligands, which have extremely small molecular size and strong chemical reducing properties, can effectively remove bulky organic ligands from the NP surface, and thus reduce the separation distance between neighboring NPs. Simultaneously, the hydrazine ligands significantly increase the number of oxygen vacancies on Fe_3O_4 and ITO NPs during LbL deposition, which markedly enhances the rate capability and capacitance of the electrodes compared to other organic ligands with bulky size and/or without reducing properties. This approach can provide a fundamental basis for developing and designing various high-performance electrochemical electrodes based on metal oxide NPs.

1. Introduction

Pseudocapacitive nanoparticles (PC NPs), which can possess a high theoretical capacity based on Faradaic redox reactions, multiple oxidation states, and a large surface-to-volume ratio, have been recognized as one of the most promising energy storage materials for resolving the low energy density of conventional supercapacitors (i.e., electric double-layer capacitors (EDLCs)) based on carbon-based materials.^[1–8] However, in most cases, their inherently low electrical conductivity leads to the sluggish charge-transfer kinetics of electrodes, resulting in much lower energy storage efficiency than the theoretically predicted one.^[6–8] In addition, the presence of various bulky/insulating organics (i.e., organic ligands bound to the surface of the NPs and/or polymeric binders) in the electrodes significantly restricts charge transfer between neighboring active materials, including the PC NPs.^[5,9–11]

Generally, the electrochemical behaviors of PC NPs are strongly affected by the size, shape, and structure as well as the intrinsic electrical conductivity of the NPs, which play a pivotal role in determining the energy storage performance of electrodes, including the rate capability and capacity.^[11–14] In particular, considering that high-quality PC NPs with controlled size and high dispersion stability in solution likely increase the active surface area, the synthesis of NPs using organic ligands with long alkyl chains (mainly fatty acids or amines) in non-polar media is more desirable than the synthesis of NPs with relatively low quality in aqueous media.^[15,16] However, the bulky organic ligands bound to the surface of NPs synthesized in non-polar media inevitably increase the separation distance between adjacent NPs and act as strong insulating barriers (or contact resistance sites) within PC NP-assembled electrodes.^[17–21] In addition, the hydrophobic properties of bulky organic ligands seriously hinder the access of reactive ions to the active NP surface for electrochemical reactions in aqueous electrolyte solutions.^[22] Although these drawbacks of bulky organic ligand-stabilized PC NPs can be alleviated to some degree by the incorporation of conductive components such as carbon nanotubes (CNTs),^[23–26] such organic ligands still act as a major obstacle in addressing the charge-transfer issues at all interfaces within the electrodes composed of small PC NPs ranging from a few to tens of nanometers in size. Moreover, most conductive

Y. Song, S. Lee, J. Huh, J. Cho
Department of Chemical and Biological Engineering
Korea University
145 Anam-ro, Seongbuk-gu, Seoul 02841, Republic of Korea
E-mail: jinhan71@korea.ac.kr

Y. Ko
Division of Energy Technology
Materials Research Institute
Daegu Gyeongbuk Institute of Science and Technology (DGIST)
333 Techno Jungang-daero, Hyeonpung-eup, Dalseong-gun, Daegu
42988, Republic of Korea

Y. Kim, J. Cho
KU-KIST Graduate School of Converging Science and Technology
Korea University
145 Anam-ro, Seongbuk-gu, Seoul 02841, Republic of Korea

B. Yeom
Department of Chemical Engineering
Hanyang University
222 Wangsimni-ro, Seongdong-gu, Seoul 04763, Republic of Korea

J. H. Moon
Department of Chemical and Biomolecular Engineering
Sogang University
35 Baekbeom-ro, Mapo-gu, Seoul 04107, Republic of Korea

 The ORCID identification number(s) for the author(s) of this article can be found under <https://doi.org/10.1002/adfm.202106438>.

DOI: 10.1002/adfm.202106438

components have been mainly limited to bulky carbon-based materials (particularly CNTs) or conducting polymers, which can notably decrease the energy density (specifically volumetric energy density) of electrodes, along with polymeric binders.^[27]

However, despite these critical issues, the charge-transfer effects of organic ligands depending on their physical and/or chemical properties have been overlooked in the last few decades and less studied than other components in PC NP-based electrodes. In particular, powder-based slurry casting methods, which have been widely used to prepare energy storage electrodes, are highly vulnerable to the aggregation and/or segregation of active materials due to the unfavorable interfacial interaction between neighboring components,^[28,29] which makes it more difficult to distinguish the organic ligand effects occurring at the nanoscale interfaces from the overall performance of the electrodes. Additionally, conventional PC materials have irregular and large sizes ranging from hundreds of nanometers to a few micrometers, which greatly limits the ability to comprehensively understand the role of organic ligands in charge transfer at the interfaces. Therefore, a delicate interfacial assembly method based on the organic ligands with controlled physical and/or chemical functionalities should be considered to clearly understand the effects of organic ligands on the charge-transfer kinetics within PC NP-based electrodes and to further develop high-performance energy storage electrodes.

Herein, we report that controlling the size/functionality and interfacial interaction of organic ligands can significantly enhance the performance of oxide NP-based pseudocapacitor electrodes. Furthermore, we demonstrate that the periodic incorporation of conductive oxide NPs into PC NP-based electrodes using chemical reducing ligand-mediated assembly can markedly activate charge transfer between neighboring PC NPs as well as between PC NPs and conductive NPs. The prepared oxide NP-based electrodes exhibited remarkably improved energy storage performance (mainly rate capability and capacity), which was in stark contrast to the electrodes containing bulky organics. To this end, pseudocapacitive iron oxide (Fe₃O₄) NPs and conductive indium tin oxide (ITO) NPs, which were synthesized using bulky organic ligands in nonpolar media, were alternately layer-by-layer (LbL)-assembled with the aid of extremely small molecular ligands composed of only two amine (NH₂) groups (hydrazine ligands) (Scheme 1). That is, bulky/hydrophobic organic ligands on the surface of oxide NPs were effectively replaced by the small hydrazine ligands via ligand exchange reaction during successive LbL assembly. The small hydrazine ligands also served as molecular linkers directly bridging adjacent NPs without the use of polymeric binder/linkers. As a result, the separation distance between vertically neighboring Fe₃O₄ NPs was decreased to ≈5.6 Å (computed by atomistic molecular dynamics (MD) simulations) by the use of small hydrazine ligands, which substantially reduced the contact resistance at the numerous NP–NP interfaces.

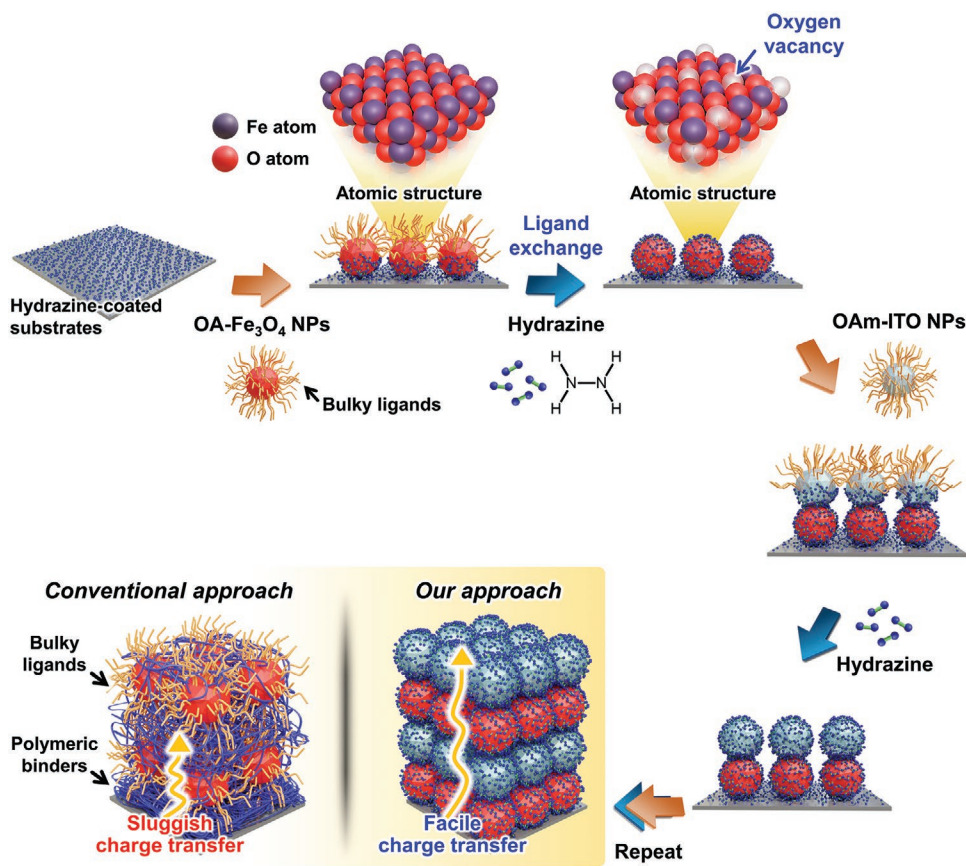
Additionally, we highlight that the strong chemical reducing properties of hydrazine ligands can induce the formation of numerous oxygen vacancy states on the pseudocapacitive and conductive oxide NPs (i.e., Fe₃O₄ and ITO NPs) through simple LbL assembly without any additional thermal and/or chemical treatments, resulting in a significant enhancement in the electrical conductivity of electrodes. Notably,

these unique phenomena were not observed for other types of organic ligands, such as poly(ethyleneimine) (PEI; i.e., bulky NH₂-functionalized ligands) and oxalic acid (OxA; i.e., small molecular ligands composed of only two carboxylic acid (COOH) groups). Another notable benefit of our approach is that the favorable interfacial interaction between the NH₂ groups of hydrazine ligands and the surface of NPs can produce nanocomposite electrodes with hierarchically nano-blended structure, controlled film thickness, and conformal coating. Therefore, the Fe₃O₄/ITO NP electrodes prepared by the hydrazine ligand-mediated LbL assembly had much higher charge-transfer efficiency and capacitance than other electrodes without hydrazine ligands or ITO NPs. Given that the size/functionality of organic ligands and the hierarchical structure of PC NP-based electrodes have decisive effects on the electrical and/or electrochemical properties, we believe that our approach can provide an insight for resolving the charge-transfer issues in a variety of other metal oxide NP-based electrochemical applications as well as pseudocapacitors.

2. Results and Discussion

2.1. Chemical Reducing Ligand-Mediated Assembly of PC NPs

For the preparation of Fe₃O₄ NP-based electrodes, oleic acid (OA)- and oleylamine (OAm)-stabilized Fe₃O₄ NPs (designated OA-Fe₃O₄ NPs) with a diameter of 6.7 ± 0.8 nm and stable dispersion in toluene (Figure 1a; Figure S1, Supporting Information) were consecutively LbL-assembled with hydrazine ligands. In this case, the hydrazine ligands composed of only two primary NH₂ groups have a higher affinity for the bare surface of oxide NPs than bulky native ligands (i.e., OA/OAm ligands) because the adsorption energy (or binding energy) of hydrazine ligands, with extremely small molecular size and bidentate binding sites, is much higher than that of bulky native ligands, with long aliphatic chains and mono-/bidentate binding sites.^[30,31] The density functional theory (DFT) calculations reported by You and co-workers also shows that the adsorption energy of organic ligands on the surface of oxide NPs becomes stronger with decreasing the hydrocarbon-chain length of ligands.^[30] Thus, the bulky native ligands loosely bound to the surface of Fe₃O₄ NPs could be easily replaced by the extremely small hydrazine ligands with thermodynamically favorable interfacial interaction during the LbL deposition of (Fe₃O₄ NP/hydrazine)_n multilayers (*n*: bilayer number), as confirmed by Fourier transform infrared (FTIR) spectroscopy (see the detailed explanation in Figure S2, Supporting Information). This ligand exchange reaction also suggested that the Fe₃O₄ NPs buried within the multilayers could be well stabilized by hydrophilic hydrazine ligands with NH₂ groups instead of by hydrophobic native ligands with long aliphatic chains. Therefore, the outermost hydrazine ligand-coated (Fe₃O₄ NP/hydrazine)_n multilayers exhibited hydrophilic surface properties with a low water contact angle of ≈35°, unlike the hydrophobic pristine OA-Fe₃O₄ NP film that had a relatively high water contact angle of ≈105° (Figure 1b). These phenomena indicate the possibility that the favorable interfaces between (Fe₃O₄ NP/hydrazine)_n multilayers and aqueous electrolytes can



Scheme 1. Schematic representation of the preparation of oxide NP-based pseudocapacitor electrodes with the periodic incorporation of conductive oxide NPs using chemical reducing ligand-mediated LbL assembly.

be formed, which leads to effective ion diffusion into the multilayers during electrochemical reactions.^[32]

On the basis of these results, we quantitatively examined the loading amount of the $(\text{Fe}_3\text{O}_4 \text{ NP/hydrazine})_n$ multilayers as a function of the bilayer number using a quartz crystal microbalance (QCM) based on the Sauerbrey equation (see the Experimental Section).^[33,34] Figure 1c shows the frequency change ($-\Delta F$) and the mass change (ΔM) (calculated from the frequency change) for the deposition of OA- Fe_3O_4 NPs and hydrazine ligands. The alternating deposition of OA- Fe_3O_4 NPs and hydrazine ligands resulted in an average ΔM of $2.19 \mu\text{g cm}^{-2}$ ($-\Delta F$ of 124 Hz) per bilayer (i.e., $(\text{Fe}_3\text{O}_4 \text{ NP/hydrazine})_1$). In this case, the decrease in ΔM during the deposition of hydrazine ligands was mainly attributed to the ligand exchange reaction between the bulky native ligands (M_w of OA $\approx 282 \text{ g mol}^{-1}$ and M_w of OAm $\approx 267 \text{ g mol}^{-1}$) and the small hydrazine ligands (M_w of hydrazine $\approx 32 \text{ g mol}^{-1}$).^[35] The uniform and regular growth of $(\text{Fe}_3\text{O}_4 \text{ NP/hydrazine})_n$ multilayers was also qualitatively monitored by UV-vis spectroscopy (Figure 1d). The total film thickness of $(\text{Fe}_3\text{O}_4 \text{ NP/hydrazine})_n$ multilayers linearly increased from ≈ 70 to 265 nm (average thickness of $\approx 6.63 \text{ nm}$ per bilayer) with increasing the bilayer number from 10 to 40, respectively, forming the densely NP-packed but nanoporous structure (Figure 1e; Figures S3 and S4, Supporting Information). Moreover, as observed by atomic force microscopy (AFM), these multilayers exhibited a highly smooth surface

morphology with a low root-mean-square (RMS) roughness of $\approx 4.43 \text{ nm}$ (Figure 1f). That is, the hydrazine ligand-mediated LbL assembly induced the formation of nanocomposite films with precisely controlled thickness (or loading amount) and highly uniform nanostructure. However, it should be noted that these ligand-controlled films cannot be prepared from the simply mixing process (i.e., blending solution process) of Fe_3O_4 NPs and hydrazine molecules. Although the ligand exchange reaction between bulky native ligands and hydrazine molecules can occur in the mixed solution, the hydrazine ligands cannot provide sufficient steric hindrance and interfacial polarity for the stable dispersion of NPs in organic media.^[36] Consequently, the hydrazine ligand-stabilized Fe_3O_4 NPs in the mixed solution were easily aggregated (Figure S5, Supporting Information), making it difficult to induce the formation of nanocomposite films with the desired chemical compositions and thickness.

In addition, the mass ratio of pure inorganic Fe_3O_4 NPs in the $(\text{Fe}_3\text{O}_4 \text{ NP/hydrazine})_n$ multilayers was estimated to be $\approx 89.3\%$ ($\approx 77.6\%$ in the case of a pristine OA- Fe_3O_4 NP film) by thermogravimetric analysis (TGA) (Figure 1g; Figure S6, Supporting Information). According to the QCM and TGA results, the loading amounts of Fe_3O_4 NPs and hydrazine ligands in the 6.63 nm-thick $(\text{Fe}_3\text{O}_4 \text{ NP/hydrazine})_1$ bilayers were measured to be ≈ 1.96 and $0.23 \mu\text{g cm}^{-2}$, respectively (the loading amount of native ligands in the OA- Fe_3O_4 NPs was

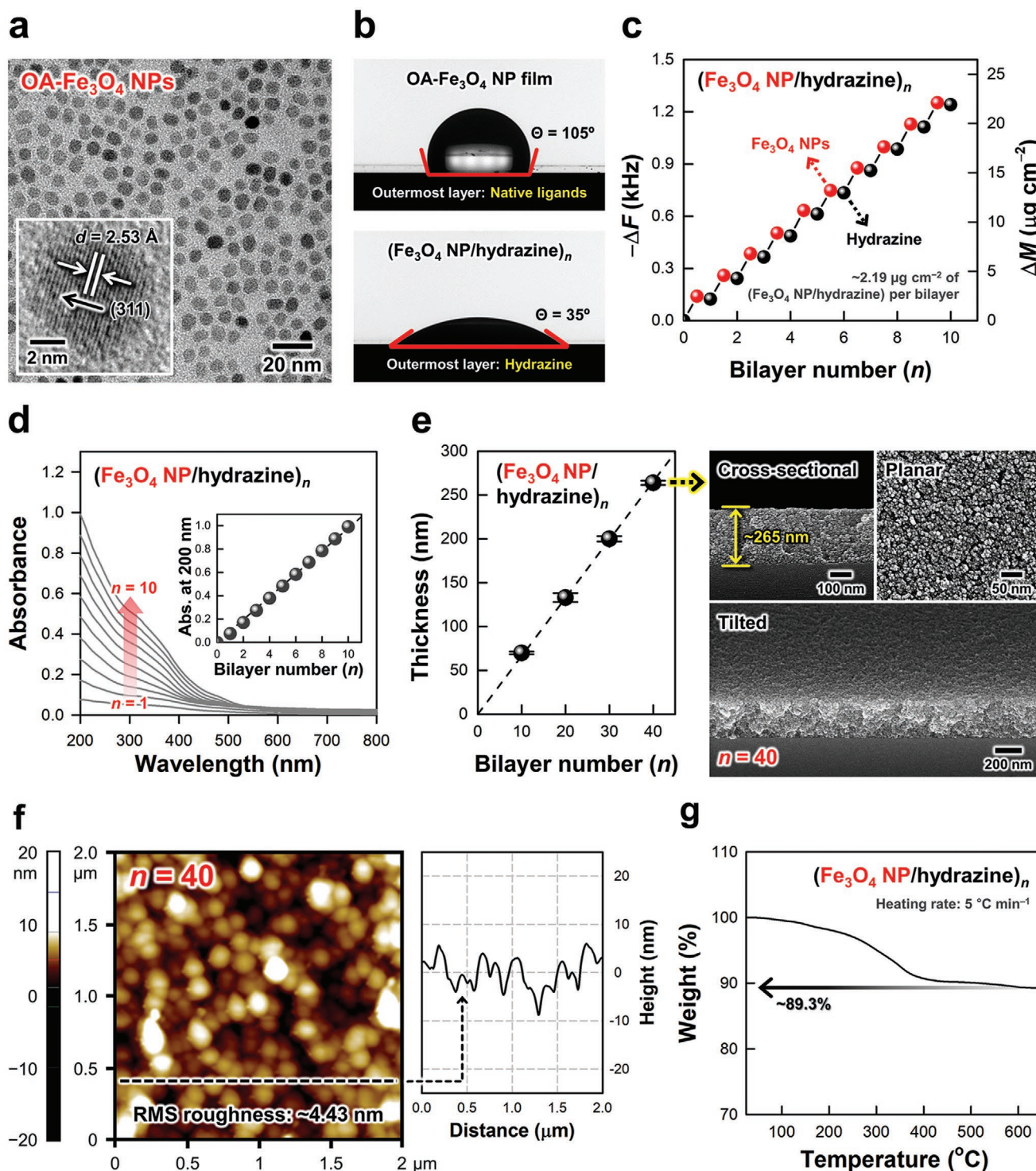


Figure 1. a) HR-TEM images of 6.7 nm-sized OA-Fe₃O₄ NPs. The inset shows a lattice spacing (d) of $\approx 2.53 \text{ \AA}$ corresponding to the (311) plane of Fe₃O₄. b) Photographs of sessile water droplets and contact angle (Θ) of a pristine OA-Fe₃O₄ NP film and (Fe₃O₄ NP/hydrazine)_n multilayers. c) Frequency change ($-\Delta F$, left axis) and mass change (ΔM , right axis) of (Fe₃O₄ NP/hydrazine)_n multilayers obtained from QCM measurements with increasing the bilayer number. The red and black circles indicate the deposition of OA-Fe₃O₄ NPs and hydrazine ligands, respectively. d) UV-vis absorbance spectra of (Fe₃O₄ NP/hydrazine)_n multilayers as the bilayer number increased from 1 to 10. The inset indicates a linear increase in the absorbance at a wavelength of 200 nm, implying regular and uniform growth of the multilayers. e) Film thickness change of (Fe₃O₄ NP/hydrazine)_n multilayers as a function of the bilayer number and cross-sectional/planar/tilted FE-SEM images of the multilayers at the bilayer number of 40. f) Two-dimensional AFM topographic images (left) and height profiles (right; obtained from the black dashed line) of (Fe₃O₄ NP/hydrazine)₄₀ multilayers in a scan area of $2 \mu\text{m} \times 2 \mu\text{m}$. g) TGA profiles of (Fe₃O₄ NP/hydrazine)_n multilayers.

$\approx 0.56 \mu\text{g cm}^{-2}$). Therefore, assuming that a single 6.7 nm-sized Fe_3O_4 NP has a spherical volume size of $\approx 1.57 \times 10^{-19} \text{ cm}^3$ and a mass density of $\approx 5.2 \text{ g cm}^{-3}$, the number density of Fe_3O_4 NPs per unit area was calculated to be $\approx 2.39 \times 10^{12} \text{ cm}^{-2}$, which corresponded to 3D packing density of $\approx 56\%$. Particularly, given that randomly close-packed NP arrays have the maximum 3D packing density of 64%,^[33] our results implied that the $(\text{Fe}_3\text{O}_4 \text{ NP/hydrazine})_n$ multilayers had the extremely high packing density of NPs, which could be also confirmed by the FE-SEM images (Figure 1e). Additionally, it should be noted that the high packing density of NPs shown in our study cannot be observed in the electrostatic LbL assembly that generates the long-range electrostatic repulsion between the same charged NPs in aqueous media.^[37–39] Generally, in the case of electrostatic LbL assembly, the packing density of adsorbed NPs per layer in lateral dimension is limited to less than 30%.^[5,33] On the other hand, our hydrazine ligand-mediated LbL assembly in organic media can produce the densely packed NP films by minimizing the separation distance without repulsion force as well as by lowering the amount of bulky organics (i.e., bulky native ligands and/or polymeric binders).

2.2. Organic Ligand-Induced Electrical Properties

To investigate the effects of size/functionality-dependent organic ligands on the electrical and electrochemical properties of electrodes, the Fe_3O_4 NP multilayers were assembled using three different types of organic ligands. In this case, bulky NH_2 -functionalized PEI and small COOH-functionalized OxA were additionally used as organic ligands (or linkers) for the comparison with hydrazine ligands (Figure 2a). The total film thicknesses of all Fe_3O_4 NP multilayers were fixed at $\approx 265 \text{ nm}$ by controlling the bilayer number (hydrazine: $n = 40$, OxA: $n = 36$, and PEI: $n = 32$) (Figure S7, Supporting Information). Additionally, a pristine OA- Fe_3O_4 NP film as a reference sample was prepared using a spin-coating method. Particularly, it should also be noted that the OxA ligands composed of only two COOH groups have a higher binding affinity with the surface of Fe_3O_4 NPs than bulky native ligands with long aliphatic chains.^[40] Thus, similar to the phenomena observed from NH_2 -functionalized ligands such as hydrazine and PEI, the COOH-functionalized OxA ligands could effectively replace bulky native ligands on the surface of Fe_3O_4 NPs during LbL deposition (Figure S8, Supporting Information).

Based on these results, the electrical properties of the $(\text{Fe}_3\text{O}_4 \text{ NP/hydrazine})_{40}$, $(\text{Fe}_3\text{O}_4 \text{ NP/OxA})_{36}$, $(\text{Fe}_3\text{O}_4 \text{ NP/PEI})_{32}$, and pristine OA- Fe_3O_4 NP films were examined using a two-probe method (an electrode contact area of $\approx 0.197 \text{ mm}^2$), as shown in Figure 2b. In particular, the pristine OA- Fe_3O_4 NP film displayed almost insulating property (extremely low current levels of $\approx 10^{-11} \text{ A}$ under an applied voltage range of $\pm 1.5 \text{ V}$) because the excess amount of bulky native ligands greatly increased the contact resistance between adjacent Fe_3O_4 NPs. On the other hand, the LbL-assembled multilayers followed the conduction mechanism relation ($J \propto E^\alpha$) between the current density (J) and the electric field (E).^[41] That is, the pristine OA- Fe_3O_4 NP film had an α value of ≈ 0.07 with

insulating property, while the LbL-assembled multilayers had an α value of ≈ 1 , indicating ohmic conduction (Figure 2c). These phenomena were mainly due to the effective removal of bulky native ligands (i.e., insulating barriers covering the Fe_3O_4 NPs) by the ligand exchange reaction, and clearly implied that organic ligands bound to the surface of NPs could play a critical role in determining the charge-transfer efficiency across the electrodes. Moreover, the electrical conductivity of the $(\text{Fe}_3\text{O}_4 \text{ NP/PEI})_{32}$ multilayers was slightly higher than that of the pristine OA- Fe_3O_4 NP film despite the higher M_w ($\approx 800 \text{ g mol}^{-1}$) of PEI ligands than of native ligands (M_w of OA $\approx 282 \text{ g mol}^{-1}$ and M_w of OAm $\approx 267 \text{ g mol}^{-1}$). These results can be explained by the fact that only one layer of PEI ligands was conformally assembled at the interfaces between adjacent Fe_3O_4 NPs as a result of the LbL assembly while several layers of bulky native ligands were formed at the interfaces in the pristine OA- Fe_3O_4 NP film.^[42]

In contrast, hydrazine ($\text{H}_2\text{N-NH}_2$, $M_w \approx 32 \text{ g mol}^{-1}$) and OxA (HOOC-COOH , $M_w \approx 90 \text{ g mol}^{-1}$) ligands, with extremely small molecular sizes, operated as favorable linkers that could markedly decrease the insulating barriers at the NP-NP interfaces. The current responses of the $(\text{Fe}_3\text{O}_4 \text{ NP/hydrazine})_{40}$ and $(\text{Fe}_3\text{O}_4 \text{ NP/OxA})_{36}$ multilayers were $\approx 10^4$ and 10^3 times higher than those of the pristine OA- Fe_3O_4 NP film, respectively, at an applied voltage of $\pm 1.5 \text{ V}$ (Figure 2b). These notable improvements in electrical properties were mainly due to the significantly shortened separation distance between neighboring Fe_3O_4 NPs with the aid of small molecular ligands. For the better understanding about these phenomena, the interparticle distance of Fe_3O_4 NPs vertically bridged by hydrazine or OxA ligands in the LbL-assembled multilayers was computed using atomistic MD simulations. The MD-optimized structures revealed that the minimal distances between hydrazine- and OxA-ligated Fe_3O_4 NPs were ≈ 5.6 and 6.8 \AA , respectively (Figure 2d). As mentioned above, the minimized separation distance could notably reduce the contact resistance at the numerous NP-NP interfaces, thereby possibly enhancing the charge transfer within the Fe_3O_4 NP multilayers. However, the current levels in the $(\text{Fe}_3\text{O}_4 \text{ NP/hydrazine})_{40}$ multilayers were at least 10 times higher than those in the $(\text{Fe}_3\text{O}_4 \text{ NP/OxA})_{36}$ multilayers despite their similar separation distances; thus, another important factor should be further considered to understand the electrical properties of the Fe_3O_4 NP multilayers.

A notable possibility is the increase in oxygen vacancy states on the surface of LbL-assembled Fe_3O_4 NPs with hydrazine ligands. It is well known that the oxygen vacancies of metal oxides can operate as n-type dopants (i.e., electronic states close to the conduction band minimum (CBM)), transforming insulating oxides into semiconducting oxides.^[43–49] That is, the generation of oxygen vacancies leaves two electrons for each missing oxygen atom, which improves the electrical conductivity of metal oxides through the increased electron carrier concentration.^[49] Particularly, given that hydrazine molecules have been widely used as strong chemical reducing agents,^[50–52] the oxygen vacancy states on the Fe_3O_4 NPs can be strongly influenced by hydrazine ligands during LbL assembly. Such a possibility was supported by X-ray photoelectron spectroscopy (XPS) analysis (Figure 2e). In the Fe 2p core-level spectra of the $(\text{Fe}_3\text{O}_4$

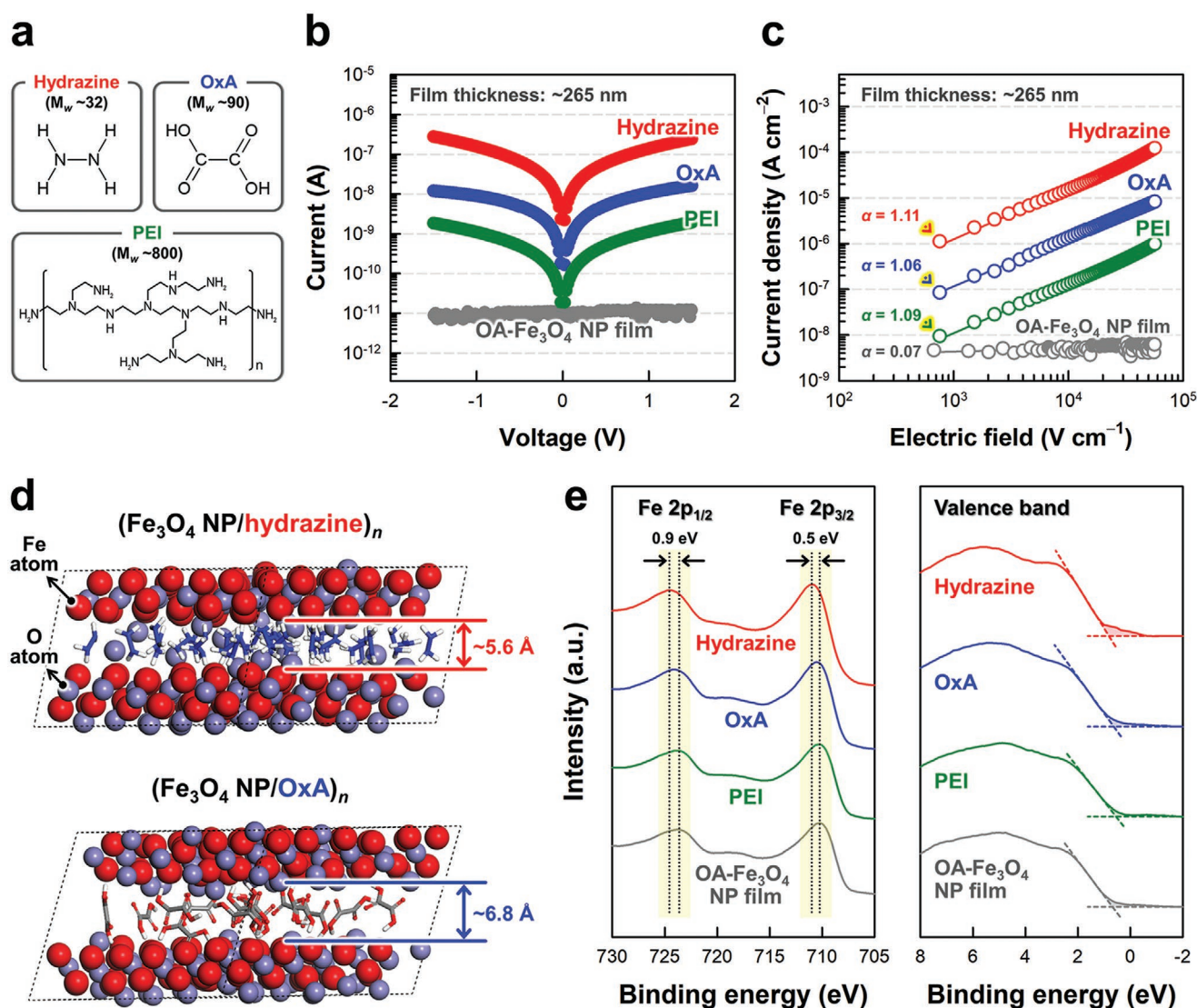


Figure 2. a) Molecular structures and weight (M_w) of hydrazine, OxA, and PEI ligands used for the preparation of Fe_3O_4 NP multilayers. b) Current (I)–voltage (V) curves and c) current density (J)–electric field (E) profiles of $(\text{Fe}_3\text{O}_4 \text{ NP/linker})_n$ multilayers (linker: hydrazine, OxA, and PEI ligands) and a pristine OA- Fe_3O_4 NP film at a similar film thickness of ≈ 265 nm. d) Atomistic MD-simulated structures of the single layer of ligand molecules (hydrazine and OxA) confined between the Fe_3O_4 NPs. e) Fe 2p core-level (left) and valence band (right) XPS spectra of $(\text{Fe}_3\text{O}_4 \text{ NP/linker})_n$ multilayers (linker: hydrazine, OxA, and PEI ligands) and a pristine OA- Fe_3O_4 NP film.

NP/hydrazine) $_n$ multilayers, the energy shifts of Fe $2p_{1/2}$ and Fe $2p_{3/2}$ peaks (0.9 and 0.5 eV, respectively) toward higher binding energies implied that the hydrazine ligands made a stronger effect on the chemical states of Fe_3O_4 NPs than did the OxA or PEI ligands. However, unfortunately, the ratio of the Fe^{2+} to Fe^{3+} (by oxygen vacancies) states of the LbL-assembled Fe_3O_4 NPs could not be directly calculated due to the overlapped binding energies of the multiple Fe^{2+} and Fe^{3+} peaks.^[53,54] As an alternative, we investigated the integral area between the baselines and the valence band maximum (VBM) cutoffs in the valence band spectra. In this case, a larger integral area indicates a higher number of electronic states close to the Fermi level from the formation of oxygen vacancy states.^[55] Therefore, considering that the integral area of the $(\text{Fe}_3\text{O}_4 \text{ NP/hydrazine})_{40}$ multilayers

was much larger than that of the $(\text{Fe}_3\text{O}_4 \text{ NP/OxA})_{36}$, $(\text{Fe}_3\text{O}_4 \text{ NP/PEI})_{32}$, and OA- Fe_3O_4 NP films, it could be concluded that the hydrazine ligands increased the number of oxygen vacancies on the surface of the Fe_3O_4 NPs without any additional thermal or chemical treatments.

2.3. Organic Ligand-Induced Electrochemical Properties

We also examined the electrochemical behaviors of $(\text{Fe}_3\text{O}_4 \text{ NP/hydrazine})_n$ multilayers on ITO glasses in a three-electrode system using a 0.5 m Na_2SO_3 electrolyte at room temperature. Cyclic voltammetry (CV) scans were first taken at a scan rate of 100 mV s^{-1} in a potential window of -1.0 to 0 V

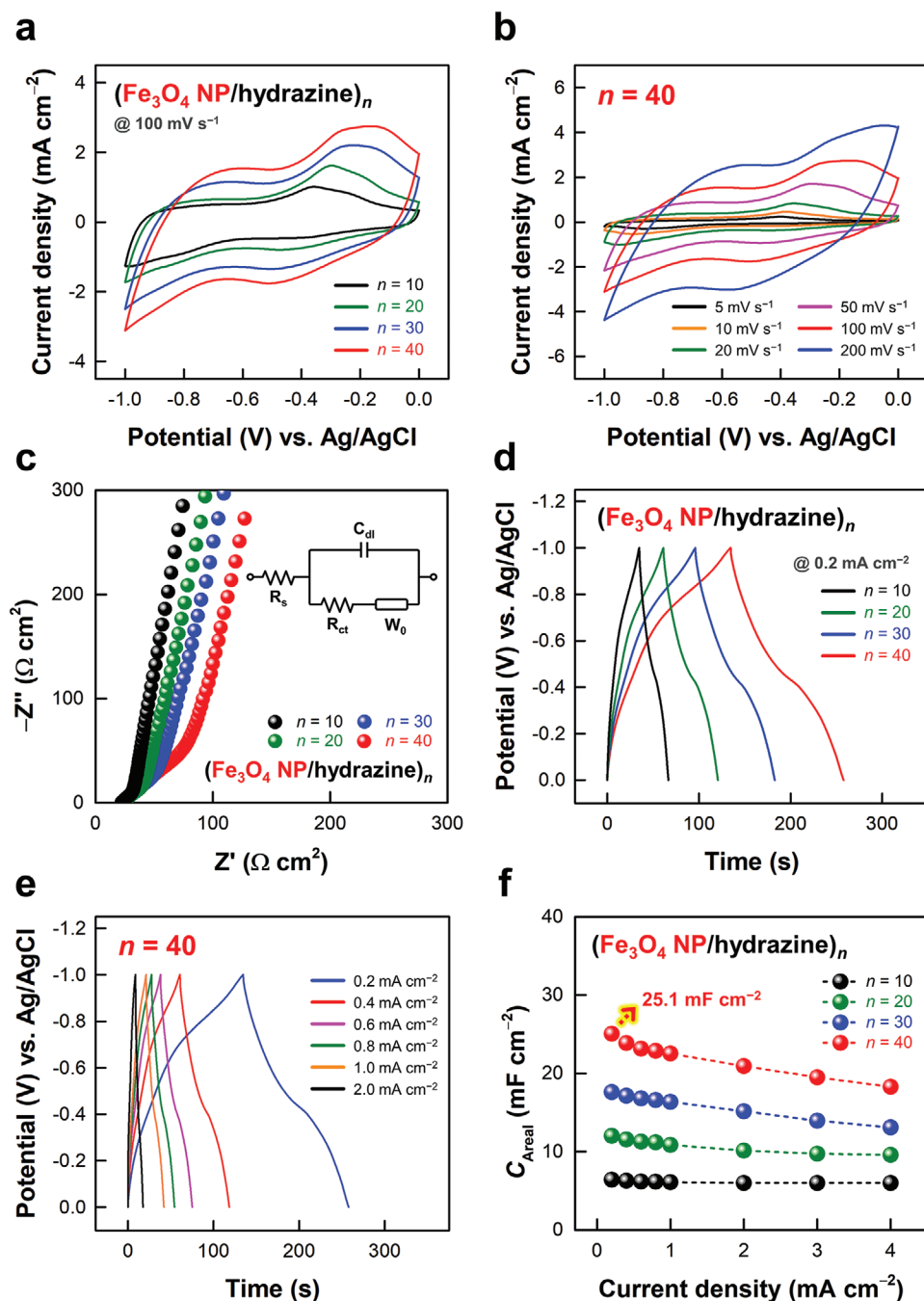
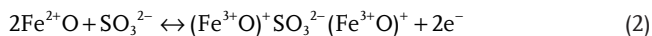
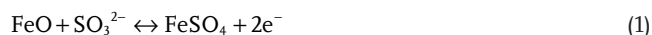


Figure 3. a) CV curves of $(\text{Fe}_3\text{O}_4 \text{ NP/hydrazine})_n$ multilayers at a scan rate of 100 mV s^{-1} as a function of the bilayer number. b) Scan rate-dependent CV curves (in the range of 5 to 200 mV s^{-1}) of $(\text{Fe}_3\text{O}_4 \text{ NP/hydrazine})_{40}$ multilayers. c) Nyquist plots, equivalent circuit (inset), and d) GCD curves at a current density of 0.2 mA cm^{-2} of $(\text{Fe}_3\text{O}_4 \text{ NP/hydrazine})_n$ multilayers with increasing the bilayer number. e) Current density-dependent GCD curves (in the range of 0.2 to 2.0 mA cm^{-2}) of $(\text{Fe}_3\text{O}_4 \text{ NP/hydrazine})_{40}$ multilayers. f) Areal capacitance (C_{Areal}) values of $(\text{Fe}_3\text{O}_4 \text{ NP/hydrazine})_n$ multilayers with varying the current density from 0.2 to 4.0 mA cm^{-2} as a function of the bilayer number.

versus a Ag/AgCl reference (Figure 3a). As the bilayer number increased from 10 (thickness of $\approx 70 \text{ nm}$) to 40 (thickness of $\approx 265 \text{ nm}$), the current responses and the resultant integral area of the CV curves gradually increased, suggesting that the charge storage capacity could be controlled by the bilayer

number. The notable redox peaks shown in the CV curves were attributed to reversible Faradaic processes based on the surface redox reactions of sulfur in the form of sulfate/sulfite anions as well as the multivalent state changes between Fe^{2+} and Fe^{3+} , accompanied by the possible intercalation of sulfite

anions.^[56] These charge storage mechanisms can be described by the following equations:



Additionally, the oxidation peaks during the anodic CV sweeps were slightly shifted toward positive potentials according to the increase of bilayer number, resulting from an increase in the internal resistance of the multilayers due to the increased loading amount (or film thickness). In particular, the $(\text{Fe}_3\text{O}_4 \text{ NP/hydrazine})_n$ multilayers exhibited evident redox peaks without significant deformation in the shape of the CV curves at different scan rates ranging from 5 to 200 mV s^{-1} (Figure 3b; Figure S9, Supporting Information). These phenomena imply that the $(\text{Fe}_3\text{O}_4 \text{ NP/hydrazine})_n$ multilayers exhibit a good rate capability due to their facile charge transfer despite the formation of densely NP-packed nanocomposite films. Furthermore, we cannot exclude the possibility that such an efficient electrochemical reaction can be partially attributed to the hydrophilic surface and the nanoporous structure of the $(\text{Fe}_3\text{O}_4 \text{ NP/hydrazine})_n$ multilayers, allowing rapid ion diffusion as mentioned earlier.

To further investigate the electrochemical behaviors of the $(\text{Fe}_3\text{O}_4 \text{ NP/hydrazine})_n$ multilayers, electrochemical impedance spectroscopy (EIS) measurements were carried out in the frequency range from 10^5 to 0.01 Hz (Figure 3c). The Nyquist plots consisted of depressed semicircles in the high-frequency region followed by straight tails in the low-frequency region, which were associated with the charge-transfer resistance (R_{ct}) and ion diffusion resistance (W_0 ; Warburg impedance) of electrodes.^[57] With increasing the bilayer number, the observed larger diameter of semicircles and the lower slope of tails implied an increase in the R_{ct} and W_0 , respectively. Specifically, when the Nyquist plots were fitted to an equivalent circuit (the inset of Figure 3c), the R_{ct} values increased from ≈ 76 to $56 \Omega \text{ cm}^2$ as the bilayer number increased from 10 to 40. Galvanostatic charge/discharge (GCD) profiles for the $(\text{Fe}_3\text{O}_4 \text{ NP/hydrazine})_n$ multilayers were also recorded to practically evaluate the charge storage capability. The GCD curves (at a current density of 0.2 mA cm^{-2}) showed the thickness-dependent pseudocapacitive behaviors, with much longer charging/discharging times with more increased bilayer number (Figure 3d), which coincided with the trend observed from the CV measurements. Additionally, the areal capacitance (C_{Areal}) values were calculated from the GCD curves obtained at various current densities from 0.2 to 4.0 mA cm^{-2} (Figure 3e; Figure S10, Supporting Information). In this case, the $(\text{Fe}_3\text{O}_4 \text{ NP/hydrazine})_n$ multilayers exhibited a C_{Areal} of $\approx 6.4 \text{ mF cm}^{-2}$ ($n = 10$) and $\approx 25.1 \text{ mF cm}^{-2}$ ($n = 40$) at a low current density of 0.2 mA cm^{-2} , and additionally, the 10- and 40-bilayered multilayers maintained $\approx 94\%$ and 73% , respectively, of their initial C_{Areal} at a high current density of 4.0 mA cm^{-2} (Figure 3f).

To further verify the effects of hydrazine ligands on the charge-transfer properties, the abovementioned electrochemical performance of the 265 nm-thick $(\text{Fe}_3\text{O}_4 \text{ NP/hydrazine})_{40}$ multilayers was compared with that of the $(\text{Fe}_3\text{O}_4 \text{ NP/OxA})_{36}$ and $(\text{Fe}_3\text{O}_4 \text{ NP/PEI})_{32}$ multilayers with the same thickness.

As shown in the CV curves at a scan rate of 100 mV s^{-1} , the $(\text{Fe}_3\text{O}_4 \text{ NP/hydrazine})_{40}$ multilayers exhibited much higher current responses with more evident redox peaks than the OxA and PEI ligand-based multilayers (Figure 4a). Additionally, despite the increased scan rates (from 5 to 200 mV s^{-1}), the redox peaks of the $(\text{Fe}_3\text{O}_4 \text{ NP/hydrazine})_{40}$ multilayers were better maintained than those of the OxA and PEI ligand-based multilayers (Figure S11, Supporting Information). These phenomena suggested that the total resistance of the $(\text{Fe}_3\text{O}_4 \text{ NP/hydrazine})_{40}$ multilayers was significantly reduced due to both the minimized interparticle distance between Fe_3O_4 NPs and the increased number of oxygen vacancies on Fe_3O_4 NPs by the hydrazine ligands, which was also clearly observed in the EIS analysis. Specifically, the $(\text{Fe}_3\text{O}_4 \text{ NP/hydrazine})_{40}$ multilayers yielded the lower R_{ct} ($\approx 56 \Omega \text{ cm}^2$) and the higher slope of tails than the OxA (R_{ct} of $\approx 97 \Omega \text{ cm}^2$) and PEI (R_{ct} of $\approx 150 \Omega \text{ cm}^2$) ligand-based multilayers (Figure 4b). The volumetric capacitance (C_{Vol}) and C_{Areal} (at a current density of 0.2 mA cm^{-2}) of the $(\text{Fe}_3\text{O}_4 \text{ NP/hydrazine})_{40}$ multilayers were determined to be $\approx 946 \text{ F cm}^{-3}$ and $\approx 25.1 \text{ mF cm}^{-2}$, respectively, which were superior to those of the OxA (C_{Vol} of $\approx 825 \text{ F cm}^{-3}$ and C_{Areal} of $\approx 21.9 \text{ mF cm}^{-2}$) and PEI (C_{Vol} of $\approx 645 \text{ F cm}^{-3}$ and C_{Areal} of $\approx 17.1 \text{ mF cm}^{-2}$) ligand-based multilayers with the same thickness of $\approx 265 \text{ nm}$ (Figure 4c; Figure S12, Supporting Information). More impressively, the $(\text{Fe}_3\text{O}_4 \text{ NP/hydrazine})_{40}$ multilayers exhibited a high capacity retention of $\approx 73\%$ even when the current densities increased to 4.0 mA cm^{-2} , which outperformed the OxA (capacity retention of $\approx 63\%$) and PEI (capacity retention of $\approx 47\%$) ligand-based multilayers (Figure 4d). These outstanding capacitance and rate capability of the $(\text{Fe}_3\text{O}_4 \text{ NP/hydrazine})_{40}$ multilayers demonstrate that hydrazine ligands can effectively promote charge transfer across the densely packed Fe_3O_4 NP arrays.

2.4. Incorporation of Conductive NPs within PC NP-Based Electrodes

Based on the hydrazine ligand-mediated LbL assembly, we tried to further enhance the energy storage performance of the Fe_3O_4 NP-based electrodes through conductive NP-incorporated hierarchical structural design. To achieve this goal, OAm and octanoic acid (OaA)-stabilized ITO NPs (designated OAm-ITO NPs) with an average diameter of $\approx 6.8 \text{ nm}$ were synthesized in toluene (Figure S13, Supporting Information), and then periodically incorporated into $(\text{Fe}_3\text{O}_4 \text{ NP/hydrazine})_n$ multilayers through the same hydrazine ligand-mediated LbL assembly (Figure 5a; Figure S14, Supporting Information). In this case, it was expected that the conductive ITO NPs could provide an effective charge-transfer pathway among the assembled Fe_3O_4 NP arrays. The regular and uniform growth of $(\text{Fe}_3\text{O}_4 \text{ NP/hydrazine/ITO NP/hydrazine})_m$ multilayers (m : period number) was quantitatively and qualitatively confirmed by both QCM (Figure 5b) and UV-vis spectroscopy (Figure 5c), respectively. The average ΔM of $(\text{Fe}_3\text{O}_4 \text{ NP/hydrazine})_1$ in the $(\text{Fe}_3\text{O}_4 \text{ NP/hydrazine/ITO NP/hydrazine})_m$ multilayers was measured to be $\approx 2.68 \mu\text{g cm}^{-2}$, which was slightly higher than that ($\approx 2.19 \mu\text{g cm}^{-2}$) of $(\text{Fe}_3\text{O}_4 \text{ NP/hydrazine})_1$ in the $(\text{Fe}_3\text{O}_4 \text{ NP/hydrazine})_n$ multilayers. Therefore, for a quantitatively exact comparison of

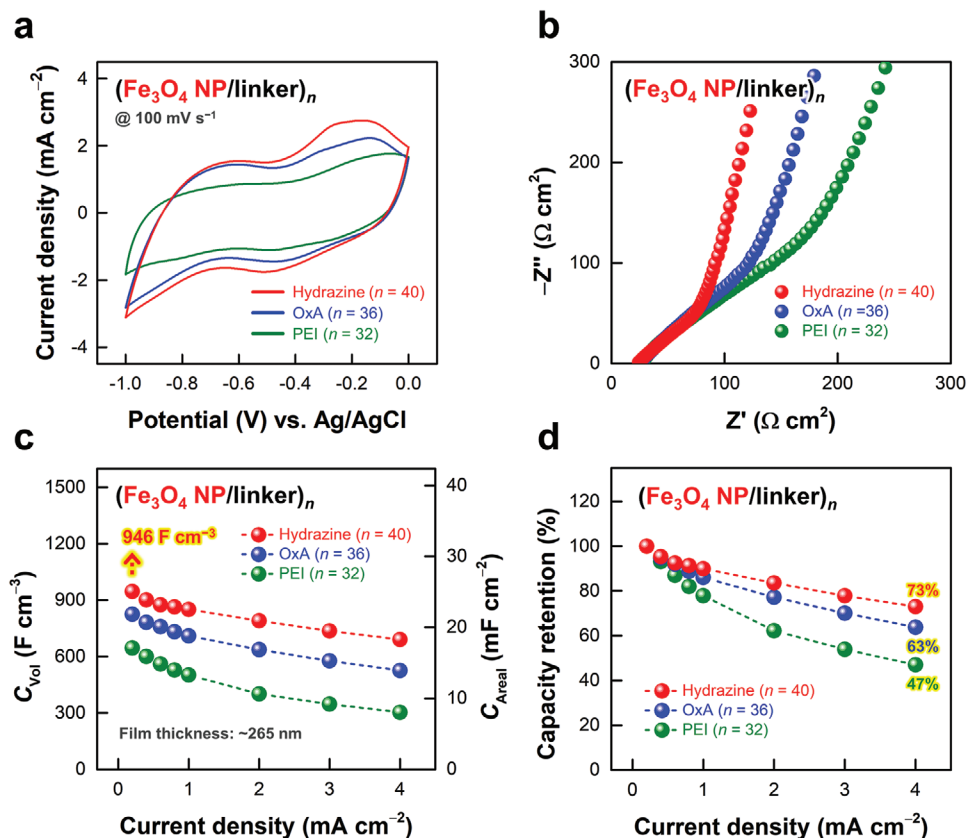


Figure 4. Comparison of a) CV curves at a scan rate of 100 mV s^{-1} and b) Nyquist plots between $(\text{Fe}_3\text{O}_4 \text{ NP/linker})_n$ multilayers (linker: hydrazine, OxA, and PEI ligands). Comparison of c) volumetric capacitance (C_{Vol} , left axis), areal capacitance (C_{Areal} , right axis), and d) capacity retention between $(\text{Fe}_3\text{O}_4 \text{ NP/linker})_n$ multilayers (linker: hydrazine, OxA, and PEI ligands) with increasing the current density from 0.2 to 4.0 mA cm^{-2} . Herein, the film thicknesses of the Fe_3O_4 NP multilayers based on three different linkers were unified to $\approx 265 \text{ nm}$ by adjusting the bilayer number.

electrical and electrochemical properties between $(\text{Fe}_3\text{O}_4 \text{ NP/hydrazine/ITO NP/hydrazine})_m$ and $(\text{Fe}_3\text{O}_4 \text{ NP/hydrazine})_n$ multilayers, the period number of the multilayers with ITO NPs was adjusted to 32 (more details are given later). The $(\text{Fe}_3\text{O}_4 \text{ NP/hydrazine/ITO NP/hydrazine})_{32}$ multilayers had a film thickness of $\approx 446 \text{ nm}$ without any aggregation or segregation between components (Figure 5d). Additionally, energy-dispersive X-ray spectroscopy (EDS) elemental mapping revealed that the Fe_3O_4 NPs and ITO NPs were homogeneously distributed within the multilayers, implying the formation of an efficient charge-transfer pathway (Figure 5e).

Importantly, the LbL-assembled ITO NPs, similar to the Fe_3O_4 NPs, were chemically reduced by the hydrazine ligands, which was evidenced by the oxygen vacancy peaks in the O 1s core-level XPS spectra of the ITO NPs. Specifically, the O 1s spectra could be classified into three deconvoluted peaks corresponding to lattice oxygen ($\approx 529.7 \text{ eV}$), oxygen vacancy states ($\approx 530.9 \text{ eV}$), and surface hydroxyl groups ($\approx 532.0 \text{ eV}$) (Figure 5f).^[58] The oxygen vacancy ratio in the pristine OAm-ITO NP film was initially measured to be $\approx 26\%$, and then increased to $\approx 36\%$ in the $(\text{ITO NP/hydrazine})_n$ multilayers. Additionally, the oxygen vacancy ratio in the $(\text{ITO NP/PEI})_n$ multilayers was measured to be $\approx 30\%$ due to the slight reducing properties of NH_2 -functionalized PEI ligands. On the other hand, the oxygen vacancy ratio in the $(\text{ITO NP/OxA})_n$

multilayers was estimated to be $\approx 26\%$, indicating that the organic ligands without reducing properties had no significant effect on the oxygen vacancy states of ITO NPs (Figure S15, Supporting Information). These results clearly demonstrate that hydrazine ligands can effectively increase the number of oxygen vacancies on Fe_3O_4 and ITO NPs, and furthermore, that our approach can be extended to other metal oxides such as TiO_x , CoO_x , and VO_x . Based on these phenomena, the current responses of the $(\text{Fe}_3\text{O}_4 \text{ NP/hydrazine/ITO NP/hydrazine})_{32}$ multilayers were $\approx 10^4$ times higher (conductivity of $\approx 8.21 \text{ S cm}^{-1}$) than those of the $(\text{Fe}_3\text{O}_4 \text{ NP/hydrazine})_{40}$ multilayers (conductivity of $\approx 2.34 \times 10^{-3} \text{ S cm}^{-1}$) despite the increased film thickness, as shown in Figure 5g. That is, the chemically reduced ITO NPs incorporated between Fe_3O_4 NP arrays remarkably improved the electrical conductivity of the Fe_3O_4 NP-based electrodes, suggesting that the ITO NP-inserted electrodes have faster charge-transfer kinetics than the ITO NP-free electrodes during electrochemical reactions.

To confirm this possibility, we investigated the electrochemical performance of Fe_3O_4 NP-based electrodes with or without ITO NPs. First, the amount of pure Fe_3O_4 NPs loaded into both electrodes was fixed at $\approx 78.2 \mu\text{g cm}^{-2}$, which was determined by QCM analysis and TGA as mentioned earlier. Additionally, the $(\text{ITO NP/hydrazine})_{32}$ multilayered film was prepared as a reference. As shown in the CV curves at a scan

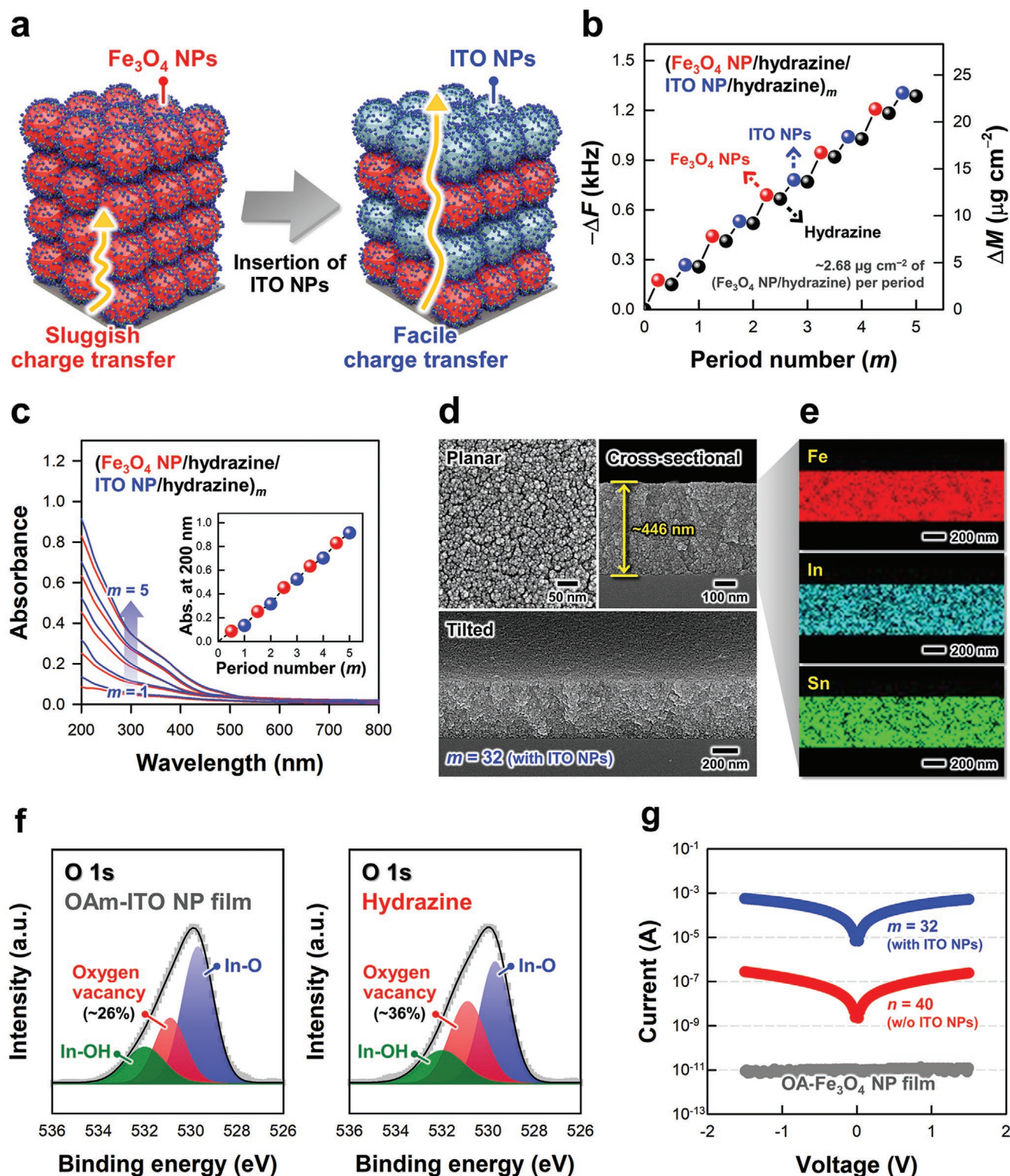


Figure 5. a) Schematic diagram of the periodic incorporation of conductive ITO NPs within the Fe_3O_4 NP multilayers. b) Frequency change ($-\Delta F$, left axis) and mass change (ΔM , right axis) of $(\text{Fe}_3\text{O}_4 \text{ NP/hydrazine/ITO NP/hydrazine})_m$ multilayers according to the deposition of OA- Fe_3O_4 NPs (red circles), hydrazine (black circles), and OAm-ITO NPs (blue circles). c) UV-vis absorbance spectra and absorbance values at a wavelength of 200 nm (inset) of $(\text{Fe}_3\text{O}_4 \text{ NP/hydrazine/ITO NP/hydrazine})_m$ multilayers with increasing the period number from 1 to 5. The red line/circles and blue line/circles indicate the deposition of $(\text{Fe}_3\text{O}_4 \text{ NP/hydrazine})_m$ multilayers and $(\text{ITO NP/hydrazine})_1$ bilayers, respectively. d) Planar/cross-sectional/tilted FE-SEM and e) EDS elemental mapping images of $(\text{Fe}_3\text{O}_4 \text{ NP/hydrazine/ITO NP/hydrazine})_{32}$ multilayers. f) O 1s core-level XPS spectra of a pristine OAm-ITO NP film (left) and $(\text{ITO NP/hydrazine})_n$ multilayers (right). g) Comparison of current ($\log I$)–voltage (V) profiles between $(\text{Fe}_3\text{O}_4 \text{ NP/hydrazine/ITO NP/hydrazine})_{32}$ and $(\text{Fe}_3\text{O}_4 \text{ NP/hydrazine})_{40}$ multilayers.

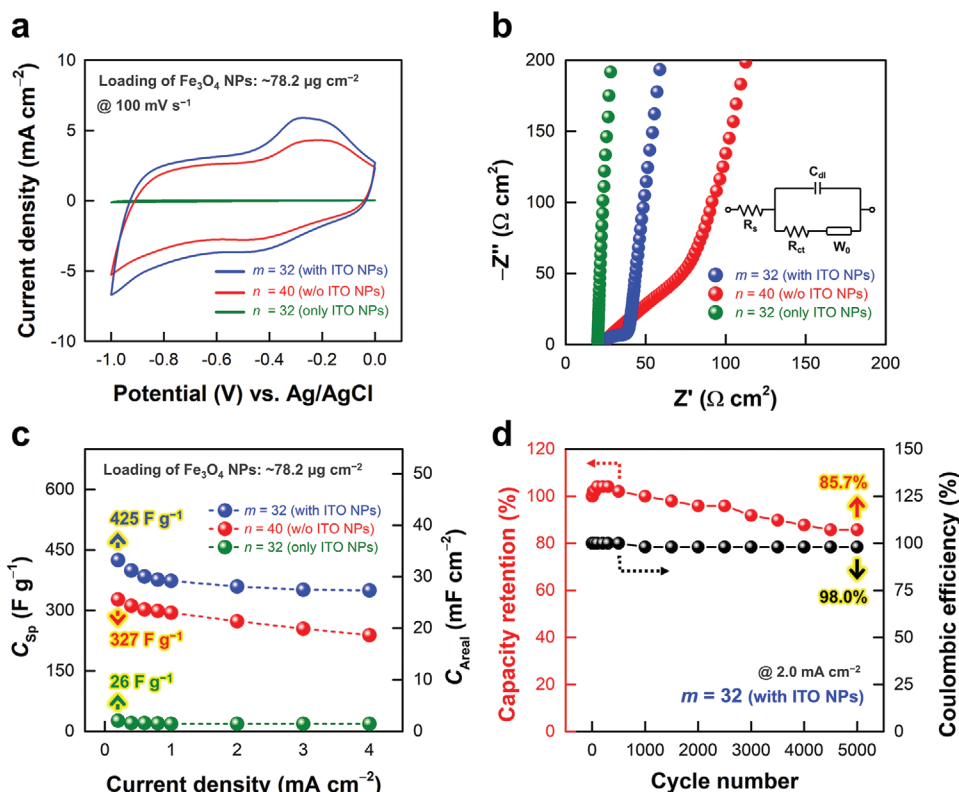


Figure 6. Comparison of a) CV curves at a scan rate of 100 mV s^{-1} , b) Nyquist plots (inset: equivalent circuit), c) specific capacitance (C_{Sp} , left axis), and areal capacitance (C_{Areal} , right axis) among $\text{Fe}_3\text{O}_4/\text{ITO}$ NP-based electrodes ($m = 32$), Fe_3O_4 NP-based electrodes without ITO NPs ($n = 40$), and $(\text{ITO NP}/\text{hydrazine})_{32}$ multilayers. Herein, the loading amount of pure Fe_3O_4 NPs in the electrodes with ITO NPs or without ITO NPs was unified to $\approx 78.2 \mu\text{g cm}^{-2}$. d) Capacity retention (left axis, red circles) and Coulombic efficiency (right axis, black circles) of $\text{Fe}_3\text{O}_4/\text{ITO}$ NP-based electrodes at a current density of 2.0 mA cm^{-2} during 5000 GCD cycles.

rate of 100 mV s^{-1} , the $\text{Fe}_3\text{O}_4/\text{ITO}$ NP-based electrodes (i.e., the 446 nm-thick $(\text{Fe}_3\text{O}_4 \text{ NP}/\text{hydrazine}/\text{ITO NP}/\text{hydrazine})_{32}$ multilayers) displayed a larger integral area than the Fe_3O_4 NP-based electrodes (i.e., the 265 nm-thick $(\text{Fe}_3\text{O}_4 \text{ NP}/\text{hydrazine})_{40}$ multilayers) (Figure 6a), which was closely related to the improved charge storage capability. On the other hand, the $(\text{ITO NP}/\text{hydrazine})_{32}$ film produced the CV curve with a negligible integral area, implying little contribution to the capacitive behaviors. Given that the separation between the redox peaks (ΔE_p ; or potential difference) of CV curves is inversely proportional to the charge-transfer rate,^[8] the decrease in the ΔE_p observed in the $\text{Fe}_3\text{O}_4/\text{ITO}$ NP-based electrodes reflected a facile charge transfer, which was mainly attributed to the insertion of conductive ITO NPs. As a further evidence of the improved charge-transfer kinetics, EIS analysis showed that the R_{ct} ($\approx 16 \Omega \text{ cm}^2$) of the $\text{Fe}_3\text{O}_4/\text{ITO}$ NP-based electrodes was substantially lower than that ($R_{\text{ct}} \approx 56 \Omega \text{ cm}^2$) of the Fe_3O_4 NP-based electrodes without ITO NPs (Figure 6b). Additionally, it should be noted that the 446 nm-thick $\text{Fe}_3\text{O}_4/\text{ITO}$ NP-based electrodes exhibited the improved ion diffusion, with a higher slope of the tail, than did the 265 nm-thick Fe_3O_4 NP-based electrodes, despite their increased film thickness by the incorporated ITO NPs. These results imply that the reduced R_{ct} is a more dominant factor than the increased ion diffusion length in determining the capacitive behaviors of electrodes.

Based on the enhanced charge-transfer properties, the $\text{Fe}_3\text{O}_4/\text{ITO}$ NP-based electrodes exhibited the good rate performance at various scan rates ranging from 5 to 200 mV s^{-1} , which was also confirmed by GCD profiles in the current density range from 0.2 to 2.0 mA cm^{-2} (Figure S16, Supporting Information).

When the capacitance values were calculated from the GCD profiles, the $\text{Fe}_3\text{O}_4/\text{ITO}$ NP-based electrodes yielded a specific capacitance (C_{Sp}) of $\approx 424 \text{ F g}^{-1}$ (based on the loading amount of pure Fe_3O_4 NPs) and a C_{Areal} of $\approx 33.2 \text{ mF cm}^{-2}$ at a current density of 0.2 mA cm^{-2} , which outperformed the performance indices of the $(\text{Fe}_3\text{O}_4 \text{ NP}/\text{hydrazine})_{40}$ electrodes (C_{Sp} of $\approx 327 \text{ F g}^{-1}$ and C_{Areal} of $\approx 25.1 \text{ mF cm}^{-2}$) and the $(\text{ITO NP}/\text{hydrazine})_{32}$ film (C_{Sp} of $\approx 26 \text{ F g}^{-1}$ and C_{Areal} of $\approx 1.4 \text{ mF cm}^{-2}$) (Figure 6c). The $\text{Fe}_3\text{O}_4/\text{ITO}$ NP-based electrodes maintained $\approx 82\%$ of their initial capacitance when the current density increased to 4.0 mA cm^{-2} , indicating the more enhanced rate capability than the Fe_3O_4 NP-based electrodes (capacity retention of $\approx 73\%$) without ITO NPs. Although the C_{Vol} ($\approx 745 \text{ F cm}^{-3}$ at 0.2 mA cm^{-2}) of the 446 nm-thick $\text{Fe}_3\text{O}_4/\text{ITO}$ NP-based electrodes was lower than that (C_{Vol} of $\approx 946 \text{ F cm}^{-3}$) of the 265 nm thick- Fe_3O_4 NP-based electrodes due to the ≈ 1.7 times thicker electrodes (by the incorporated ITO NPs), a slight decrease ($\approx 21\%$) in the C_{Vol} of the $\text{Fe}_3\text{O}_4/\text{ITO}$ NP-based electrodes indicated that the enhanced charge-transfer kinetics could minimize the

thickness-dependent capacitance loss. Additionally, the (ITO NP/hydrazine)₃₂ film also possessed charge storage capability although the capacitance values were significantly lower than those of the other electrodes. These results were attributed to EDLC behavior of ITO NPs,^[59] as confirmed by the quasi-rectangular shaped CV curves without evident redox peaks (Figure S17, Supporting Information).

We also investigated the electrochemical stability of the Fe₃O₄/ITO NP-based electrodes through GCD cycling at a current density of 2 mA cm⁻². In this case, with increasing GCD cycling number, the size of Fe₃O₄ NP clusters was gradually increased (Figure S18, Supporting Information), which was attributed to the structural rearrangement by slight volume expansion of Fe₃O₄ NPs during repetitive surface redox reactions. However, it should be noted that these electrodes maintained their overall structure and film thickness without any notable delamination, and resultantly exhibited ≈85.7% of initial capacitance with ≈98% of Coulombic efficiency even after 5000 GCD cycles (Figure 6d). This good cycling performance evidently implied the formation of robust and stable adsorption between the hydrazine ligands and the oxide NPs. A slight increase in the capacity retention (*C*/*C*₀) at the beginning of GCD cycling was caused by the increased effective surface area between the active Fe₃O₄ NPs and the electrolytes during the electrochemical cycling.^[60] As a result, our approach using chemical reducing ligand-mediated LbL assembly could notably improve the charge-transfer efficiency by controlling the size/functionality of organic ligands bound to the surface of oxide NPs, resulting in a significant enhancement in capacitance and rate capability.

3. Conclusion

In this study, we described how the size, chemical functionalities, and interfacial interaction of organic ligands affect the performance of oxide NP-based pseudocapacitor electrodes. We also demonstrated that the charge-transfer efficiency of high-energy Fe₃O₄ NPs and conductive ITO NPs could be significantly enhanced by chemical reducing ligand-mediated LbL assembly. When hydrazine ligands, with the extremely small molecular size and strong chemical reducing properties, were LbL-assembled with OA-Fe₃O₄ NPs and OAm-ITO NPs, bulky native ligands were replaced by the hydrazine ligands, which dramatically decreased the separation distance between adjacent NPs, and furthermore increased the number of oxygen vacancies on the oxide NPs without additional thermal and/or chemical treatments. As a result, the hydrazine ligand-mediated Fe₃O₄/ITO NP electrodes exhibited significantly improved charge transfer, which greatly contributed to the enhancement in energy storage performance (mainly rate capability and capacity). Although the film thickness of the LbL-assembled electrodes in our study was relatively thin compared to that of conventional slurry-casted electrodes, we believe that our approach can provide a basis for fully understanding the interfacial charge-transfer effects of organic ligands on the oxide NP-based electrodes and developing high-performance energy storage devices with optimal electrode structures.

4. Experimental Section

Materials: Iron(III) acetylacetonate (97%), 1,2-hexadecanediol (90%), oleic acid (OA, 90%), oleylamine (OAm, 70%), benzyl ether (98%), indium(III) acetate (99.99%), tin(II) ethylhexanoate (92.5–100.0%), octanoic acid (OxA, ≥99%), dioctyl ether (99%), hydrazine hydrate solution (78–82%), oxalic acid (OxA, ≥99.0%), poly(ethyleneimine) (PEI, branched, *M*_w ≈ 800), and sodium sulfite (Na₂SO₃, ≥98%) were purchased from Sigma-Aldrich. Organic solvents (toluene, acetone, and ethanol) were obtained from Daejung Chemicals & Metals (Republic of Korea). All chemical reagents were used as received without further purification.

Synthesis of OA-Fe₃O₄ NPs: OA-Fe₃O₄ NPs were prepared as previously reported.^[61] Iron(III) acetylacetonate (2 mmol), 1,2-hexadecanediol (10 mmol), OA (6 mmol), OAm (6 mmol), and benzyl ether (20 mL) were loaded in a three-neck flask under a flow of Ar gas and with magnetic stirring. The reaction mixture was then heated at 200 °C for 2 h and further heated at 300 °C to reflux for 1 h. Upon completion of the reaction, the flask was removed from the heat source and cooled to room temperature. Then, the black mixture was purified by adding excess ethanol, followed by centrifugation (8000 rpm, 10 min, 20 °C). The precipitated OA-Fe₃O₄ NPs were redissolved in toluene containing OA (0.05 mL) and OAm (0.05 mL). Finally, centrifugal purification with ethanol was repeated several times, and the OA-Fe₃O₄ NPs in toluene were obtained.

Synthesis of OAm-ITO NPs: OAm-ITO NPs with a target tin (Sn) doping concentration of 10% were synthesized by a method similar to that reported in the literature.^[62] A mixture of indium(III) acetate (6.48 mmol), tin(II) ethylhexanoate (0.72 mmol), OAm (60 mmol), OxA (21.6 mmol), and dioctyl ether (60 mL) was magnetically stirred in a three-neck flask and heated at 80 °C for 1 h under vacuum. Next, the reaction mixture was heated at 150 °C for 1 h and then at 280 °C for 2 h under an Ar atmosphere. After cooling the flask to room temperature, centrifugal purification (8000 rpm, 10 min, 20 °C) with excess acetone was carried out several times to separate pure OAm-ITO NP precipitates that could be dispersed in toluene.

LbL Assembly of (Fe₃O₄ or ITO NP/linker)_n Multilayers: All experimental procedures for the LbL assembly were performed in a fume hood for safety. The concentrations of NPs in toluene and of organic ligands in ethanol were both adjusted to 10 mg mL⁻¹. All substrates, including Si wafers, gold-sputtered Si wafers, quartz glasses, QCM electrodes, and ITO glasses, were irradiated with a UV ozone cleaner for 30 min. Organic ligands were deposited on these surface-treated substrates to form a robust underlayer, and the surfaces were then washed twice with pure ethanol to remove weakly adsorbed materials using a spin-coating method at 2000 rpm for 30 s. The NPs (followed by washing with pure toluene) and organic ligands (followed by washing with pure ethanol) were sequentially deposited on the ligand-coated substrates to produce one bilayer of (Fe₃O₄ or ITO NP/linker)₁ under the same spin-coating conditions. These cycles (i.e., the sequential deposition of NPs and organic ligands) were repeated until the desired layer number of (Fe₃O₄ or ITO NP/linker)_n multilayers was achieved.

Characterization: The size/shape and crystal structure of NPs were observed by HR-TEM (Tecnai 20, FEI), and the crystallinity was also confirmed by XRD (SmartLab, Rigaku) with Cu K_α radiation (9 kW). FTIR analysis of multilayers on gold-sputtered Si wafers was conducted using a Cary 600 (Agilent Technologies) in attenuated total reflection (ATR) mode with a resolution of 2 cm⁻¹, and the raw spectra were plotted after baseline correction and smoothed by spectral analysis software (OMNIC, Thermo Fisher Scientific). The water contact angle was measured by a sessile drop method using a Phoenix-300 instrument (SEO Corp.) equipped with a video capture camera. The quantitative analysis of multilayers on the QCM electrodes was carried out with a QCM 200 (SRS). In this case, the mass change (ΔM , $\mu\text{g cm}^{-2}$) of multilayers was acquired from the frequency change ($-\Delta F$, Hz) using the Sauerbrey Equation (3) as follows.^[33]

$$\Delta F(\text{Hz}) = -\frac{2F_0^2}{A\sqrt{\rho_q\mu_q}} \times \Delta M \quad (3)$$

In Equation (3), F_0 is the fundamental resonance frequency (≈ 5 MHz), A is the surface area (cm^2), ρ_q is the density ($\approx 2.65 \text{ g cm}^{-3}$), and μ_q is the shear modulus ($\approx 2.95 \times 10^{11} \text{ g cm}^{-1} \text{ s}^{-2}$) of the QCM electrodes. By substituting the actual values into the parameters, Equation (3) can be expressed as Equation (4).

$$-\Delta F = 56.6 \times \Delta M \quad (4)$$

The UV-vis absorbance spectra of multilayers on quartz glass were monitored using a Lambda 35 spectrometer (Perkin Elmer) across wavelengths ranging from 200 to 1000 nm. The film thicknesses, surface morphology, and EDS elemental mapping of multilayers on Si wafers were investigated by FE-SEM (S-4800, Hitachi). The surface morphology of multilayers was scanned by AFM (XE-100, Park Systems) in tapping mode. The ratio of pure Fe_3O_4 NPs within the multilayers was analyzed by TGA (Q50, TA Instruments) with a heating rate of $5 \text{ }^\circ\text{C min}^{-1}$ under a N_2 atmosphere. The current ($\log I$)-voltage (V) profiles of multilayers were recorded by a two-probe method with a current compliance of 0.1 mA using a semiconductor parametric analyzer (Agilent 4155B, Agilent Technologies), and gold wires with a diameter of 0.5 mm were used as the top/bottom electrodes. The binding energy of multilayers Si wafers was examined by XPS (X-tool, ULVAC-PHI) with $\text{Al K}\alpha$ radiation (24.1 W).

Atomistic MD Simulations: To compute the separation distance between the LbL-assembled Fe_3O_4 NPs bridged by hydrazine or OxA ligands, atomistic MD simulations were carried out for a model system composed of ligand molecules confined between two Fe_3O_4 (100) surfaces. The molecular geometries were initially prepared by placing hydrazine or OxA ligands between the Fe_3O_4 slabs, which were arranged with a face-centered cubic (FCC) stacking with a (100) face consisting of a 3×3 supercell. Based on this model system configuration, NPT-ensemble MD simulations were conducted at 298 K and 1 bar using the COMPASS force field^[63] (COMPASS III) with the atomic charges assigned from the ESP calculations using DMOL3. A Nose-Hoover-Langevin thermostat^[64] and Parrinello-Rahman barostat^[65] were used to maintain the temperature (298 K) and pressure (1 bar). For all NPT MD runs, the electrostatic potential energy was calculated by the Ewald summation method with an accuracy of $0.1 \text{ kcal mol}^{-1}$ and a buffer width of 0.5 \AA . Additionally, van der Waals potential energy was calculated by the atom-based technique with a cutoff distance of 12.5 \AA and a spline width of 1 \AA . The MD system was equilibrated for 2 ns with a time step of 1 fs.

Electrochemical Measurements: CV, GCD, and EIS measurements were carried out with an Ivium-n-Stat analyzer (Ivium Technologies, Netherlands). A three-electrode system was applied to evaluate the electrochemical performance of working electrodes (active area of $\approx 2 \text{ cm}^2$) in the aqueous electrolyte of Na_2SO_3 (0.5 mol L^{-1}) at room temperature. In this case, commercial ITO glasses (sheet resistance of $\approx 20 \text{ } \Omega \text{ sq}^{-1}$) were used as current collectors for working electrodes. The Ag/AgCl electrodes saturated with NaCl in deionized water (3 mol L^{-1}) and Pt wires were used as the reference and counter electrodes, respectively. CV and GCD curves were acquired in the potential range between -1.0 and 0 V . EIS measurements were conducted over frequencies ranging from 10^5 to 0.1 Hz under a perturbation amplitude of 10 mV . The R_{ct} values were obtained by fitting the Nyquist plots to an equivalent circuit composed of solution resistance (R_s), R_{ct} , W_0 , and double-layer capacitance (C_{dl}) using ZView software (Scribner Associates Inc.) The capacitance (C) values were calculated from the GCD profiles according to the following Equation (5):^[66]

$$C = \frac{I \Delta t}{\Delta V} \quad (5)$$

where I , Δt , and ΔV are the applied current density, discharging time, and operating potential window, respectively. The variable (S) indicates the area of the active electrodes (C_{Areal}), the volume of the active electrodes (C_{Vol}), or the mass of the active materials (C_{Sp}).

Supporting Information

Supporting Information is available from the Wiley Online Library or from the author.

Acknowledgements

This work was supported by the National Research Foundation of Korea (NRF) grant funded by the Korea government (MSIT; Ministry of Science and ICT) (NRF-2019R1A4A1027627 and NRF-2021R1A2C3004151).

Conflict of Interest

The authors declare no conflict of interest.

Data Availability Statement

Research data are not shared.

Keywords

chemical reducing ligands, energy storage, pseudocapacitors

Received: July 5, 2021

Revised: August 18, 2021

Published online: September 9, 2021

- [1] P. Simon, Y. Gogotsi, B. Dunn, *Science* **2014**, *343*, 1210.
- [2] C. Choi, D. S. Ashby, D. M. Butts, R. H. DeBlock, Q. Wei, J. Lau, B. Dunn, *Nat. Rev. Mater.* **2020**, *5*, 5.
- [3] Q. Zhang, E. Uchaker, S. L. Candelaria, G. Cao, *Chem. Soc. Rev.* **2013**, *42*, 3127.
- [4] Q. Liao, N. Li, S. Jin, G. Yang, C. Wang, *ACS Nano* **2015**, *5*, 5310.
- [5] Y. Ko, M. Kwon, W. K. Bae, B. Lee, S. W. Lee, J. Cho, *Nat. Commun.* **2017**, *8*, 536.
- [6] S. Fleischmann, J. B. Mitchell, R. Wang, C. Zhan, D. Jiang, V. Presser, V. Augustyn, *Chem. Rev.* **2020**, *120*, 6738.
- [7] J. Jiang, Y. Li, J. Liu, X. Huang, C. Yuan, X. W. Lou, *Adv. Mater.* **2012**, *24*, 5166.
- [8] V. Augustyn, P. Simon, B. Dunn, *Energy Environ. Sci.* **2014**, *7*, 1597.
- [9] L. Zhang, X. Qin, S. Zhao, A. Wang, J. Luo, Z. L. Wang, F. Kang, Z. Lin, B. Li, *Adv. Mater.* **2020**, *32*, 1908445.
- [10] Y. Song, D. Kim, S. Kang, Y. Ko, J. Ko, J. Huh, Y. Ko, S. W. Lee, J. Cho, *Adv. Funct. Mater.* **2019**, *29*, 1806584.
- [11] Y. Ko, C. H. Kwon, S. W. Lee, J. Cho, *Adv. Mater.* **2020**, *32*, 2001924.
- [12] R. Wang, J. Lang, Y. Liu, Z. Lin, X. Yan, *NPG Asia Mater.* **2015**, *7*, 183.
- [13] T. C. Narayan, A. Baldi, A. L. Koh, R. Sinclair, J. A. Dionne, *Nat. Mater.* **2016**, *15*, 768.
- [14] K. A. Owusu, L. Qu, J. Li, Z. Wang, K. Zhao, C. Yang, K. M. Herculé, C. Lin, C. Shi, Q. Wei, L. Zhou, L. Mai, *Nat. Commun.* **2017**, *8*, 14264.
- [15] J. Park, J. Joo, S. G. Kwon, Y. Jang, T. Hyeon, *Angew. Chem., Int. Ed.* **2007**, *46*, 4630.
- [16] A. Dong, X. Ye, J. Chen, Y. Kang, T. Gordon, J. M. Kikkawa, C. B. Murray, *J. Am. Chem. Soc.* **2011**, *133*, 998.
- [17] J.-Y. Kim, N. A. Kotov, *Chem. Mater.* **2014**, *26*, 134.
- [18] D. Nam, M. Kwon, Y. Ko, J. Huh, S. W. Lee, J. Cho, *Appl. Phys. Rev.* **2021**, *8*, 011405.
- [19] S. Cong, Y. Tian, Q. Li, Z. Zhao, F. Geng, *Adv. Mater.* **2014**, *26*, 4260.

- [20] Y. Song, J. Cho, *Nanoscale* **2020**, *12*, 20141.
- [21] S. Lee, Y. Song, Y. Ko, Y. Ko, J. Ko, C. H. Kwon, J. Huh, S.-W. Kim, B. Yeom, J. Cho, *Adv. Mater.* **2020**, *32*, 1906460.
- [22] J. G. Smith, P. K. Jain, *J. Am. Chem. Soc.* **2016**, *138*, 6765.
- [23] F. E. S. Oztuna, O. Unal, E. Erdem, H. Y. Acar, U. Unal, *J. Phys. Chem. C* **2019**, *123*, 3393.
- [24] C. Zhang, T. M. Higgins, S.-H. Park, S. E. O'Brien, D. Long, J. N. Coleman, V. Nicolosi, *Nano Energy* **2016**, *28*, 495.
- [25] J. Wu, X. Gao, H. Yu, T. Ding, Y. Yan, B. Yao, X. Yao, D. Chen, M. Liu, L. Huang, *Adv. Funct. Mater.* **2016**, *26*, 6114.
- [26] Y. Ko, D. Shin, B. Koo, S. W. Lee, W.-S. Yoon, J. Cho, *Nano Energy* **2015**, *12*, 612.
- [27] W. Ma, W. Li, M. Li, Q. Mao, Z. Pan, J. Hu, X. Li, M. Zhu, Y. Zhang, *Adv. Funct. Mater.* **2021**, *31*, 2100195.
- [28] Y. Lin, X. Wang, G. Qian, J. J. Watkins, *Chem. Mater.* **2014**, *26*, 2128.
- [29] D. Bresser, D. Buchholz, A. Moretti, A. Varzi, S. Passerini, *Energy Environ. Sci.* **2018**, *11*, 3096.
- [30] H. You, W. Wang, S. Yang, *ACS Appl. Mater. Interfaces* **2014**, *6*, 19035.
- [31] B. C. Mei, K. Susumu, I. L. Medintz, H. Mattoussi, *Nat. Protoc.* **2009**, *4*, 412.
- [32] J. Zhao, H. Lai, Z. Lyu, Y. Jiang, K. Xie, X. Wang, Q. Wu, L. Yang, Z. Jin, Y. Ma, J. Liu, Z. Hu, *Adv. Mater.* **2015**, *27*, 3541.
- [33] Y. Ko, H. Baek, Y. Kim, M. Yoon, J. Cho, *ACS Nano* **2013**, *7*, 143.
- [34] Y. Lvov, K. Ariga, T. Kunitake, *Chem. Lett.* **1994**, *23*, 2323.
- [35] S. Kang, D. Nam, J. Choi, J. Ko, D. Kim, C. H. Kwon, J. Huh, J. Cho, *ACS Appl. Mater. Interfaces* **2019**, *11*, 12032.
- [36] K. J. Si, Y. Chen, Q. Shi, W. Cheng, *Adv. Sci.* **2018**, *5*, 1700179.
- [37] N. A. Kotov, I. Dékány, J. H. Fendler, *J. Phys. Chem.* **1995**, *99*, 13065.
- [38] J. Schmitt, G. Decher, W. J. Dressick, S. L. Brandow, R. E. Geer, R. Shashidhar, J. M. Calvert, *Adv. Mater.* **1997**, *9*, 61.
- [39] Y. Kim, J. Zhu, B. Yeom, M. D. Prima, X. Su, J.-G. Kim, S. J. Yoo, C. Uher, N. A. Kotov, *Nature* **2013**, *500*, 59.
- [40] M. H. Zarghami, Y. Liu, M. Gibbs, E. Gebremichael, C. Webster, M. Law, *ACS Nano* **2010**, *4*, 2475.
- [41] Y. Ko, M. Kwon, Y. Song, S. W. Lee, J. Cho, *Adv. Funct. Mater.* **2018**, *28*, 1804926.
- [42] B. Lee, K. Littrell, Y. Sha, E. V. Shevchenko, *J. Am. Chem. Soc.* **2019**, *141*, 16651.
- [43] G. Wang, Y. Yang, D. Han, Y. Li, *Nano Today* **2017**, *13*, 23.
- [44] T. Ling, P. Da, X. Zheng, B. Ge, Z. Hu, M. Wu, X.-W. Du, W.-B. Hu, M. Jaroniec, S.-Z. Qiao, *Sci. Adv.* **2018**, *4*, eaau6261.
- [45] J. Yang, X. Xiao, P. Chen, K. Zhu, K. Cheng, K. Ye, G. Wang, D. Cao, J. Yan, *Nano Energy* **2019**, *58*, 455.
- [46] S. Yang, Y. Liu, Y. Hao, X. Yang, W. A. Goddard, X. L. Zhang, B. Cao, *Adv. Sci.* **2018**, *5*, 1700659.
- [47] S. Liu, Y. Yin, D. Ni, K. S. Hui, M. Ma, S. Park, K. N. Hui, C.-Y. Ouyang, S. C. Jun, *Energy Storage Mater.* **2019**, *22*, 384.
- [48] X. Lu, Y. Zeng, M. Yu, T. Zhai, C. Liang, S. Xie, M.-S. Balogun, Y. Tong, *Adv. Mater.* **2014**, *26*, 3148.
- [49] H.-S. Kim, J. B. Cook, H. Lin, J. S. Ko, S. H. Tolbert, V. Ozolins, B. Dunn, *Nat. Mater.* **2017**, *16*, 454.
- [50] X. Gao, J. Jang, S. Nagase, *J. Phys. Chem. C* **2010**, *114*, 832.
- [51] Y. Wang, W. Lai, N. Wang, Z. Jiang, X. Wang, P. Zou, Z. Lin, H. J. Fan, F. Kang, C.-P. Wong, C. Yang, *Energy Environ. Sci.* **2017**, *10*, 941.
- [52] T. Gakhar, A. Hazra, *Nanoscale* **2020**, *12*, 9082.
- [53] D. Wilson, M. A. Langell, *Appl. Surf. Sci.* **2014**, *303*, 6.
- [54] Q. An, F. Lv, Q. Liu, C. Han, K. Zhao, J. Sheng, Q. Wei, M. Yan, L. Mai, *Nano Lett.* **2014**, *14*, 6250.
- [55] M. Rioult, D. Stanescu, E. Fonda, A. Barbier, H. Magnan, *J. Phys. Chem. C* **2016**, *120*, 7482.
- [56] V. D. Nithya, N. S. Arul, *J. Mater. Chem. A* **2016**, *4*, 10767.
- [57] S.-Y. Lu, M. Jin, Y. Zhang, Y.-B. Niu, J.-C. Gao, C. M. Li, *Adv. Energy Mater.* **2018**, *8*, 1702545.
- [58] S. Y. Lee, J. Kim, A. Park, J. Park, H. Seo, *ACS Nano* **2017**, *11*, 6040.
- [59] S. Bellani, L. Najafi, G. Tullii, A. Ansaldo, R. Oropesa-Nuñez, M. Prato, M. Colombo, M. R. Antognazza, F. Bonaccorso, *J. Mater. Chem. A* **2017**, *5*, 25177.
- [60] K. Xu, W. Li, Q. Liu, B. Li, X. Liu, L. An, Z. Chen, R. Zou, J. Hu, *J. Mater. Chem. A* **2014**, *2*, 4795.
- [61] S. Sun, H. Zeng, D. B. Robinson, S. Raoux, P. M. Rice, S. X. Wang, G. Li, *J. Am. Chem. Soc.* **2004**, *126*, 273.
- [62] M. Kanehara, H. Koike, T. Yoshinaga, T. Teranishi, *J. Am. Chem. Soc.* **2009**, *131*, 17736.
- [63] H. Sun, *J. Phys. Chem. B* **1998**, *102*, 7338.
- [64] A. A. Samoletov, C. P. Dettmann, M. A. J. Chaplain, *J. Stat. Phys.* **2007**, *28*, 1321.
- [65] M. Parrinello, A. Rahman, *J. Appl. Phys.* **1981**, *52*, 7182.
- [66] S. Zhang, N. Pan, *Adv. Energy Mater.* **2015**, *5*, 1401401.